Resistance to Optical Distortions in Three-dimensional Interferometric Temporal Focusing Microscopy

Qiyuan Song (D3)

Abstract

We analyze how optical distortions in deep imaging or dense scattering media influence three-dimensional interferometric temporal focusing (3D-ITF) imaging, and derive the distorted point spread function (PSF) and optical transfer function (OTF). Upon this, we find that 3D-ITF microscopy is less affected by optical distortions in terms of spatial resolution, artifacts and sectioning ability. Temporal focusing (TF) illumination supports a robust spatial modulation in 3D-ITF microscopy with distorted optics. As the modulation spatial frequencies are unique, they offer a redundancy in 3D-ITF microscopy. The redundancy in the spatial frequency of 3D-ITF images compensates for the loss of spatial frequency caused by the optical distortion in emission OTF. The redundancy recovers the high spatial frequencies to prevent the degradation of spatial resolution. Moreover, the redundancy recovers the distortion in the emission OTF spectrum, which causes distorted shapes in the PSF such as side lobes and double peaks. Thus, there is a relatively lossless OTF spectrum in 3D-ITF compared to TF, and this leads to better trade-off between remaining noise artifacts and resolution after Wiener filter correction.

1. Introduction

Temporal focusing (TF) technique utilizes a spatiotemporal modulation to gradually stretch the illumination laser pulse width out-of-focus. Therefore, TF offers an optical sectioning for wide-field multi-photon excitation fluorescence imaging [1-7]. On the other hand, structured illumination microscopy (SIM) [8-14] utilizes a spatially modulated illumination to down-convert the spatial frequencies beyond diffraction limitation in a raw image and then gives phase shifts in the modulation to form multiple raw images. SIM post-processes the raw images in order to separate the sub-images with different modulation frequencies and separately up-convert them. By combining the up-converted sub-images, SIM offers a spatial resolution beyond diffraction limitation and/or supports optical sectioning and/or removes background. It is convenient to combine TF and SIM via a digital micromirror device (DMD), which could be regarded as a blazed grating printed with programmable pattern. This combination [15,16], which we call interferometric temporal focusing (ITF) technique, is a win-win solution for both TF and SIM. It removes the scattered and out-of-focus emission in TF imaging through post-processing, while also reducing both the out-of-focus excitation in SIM raw images and the corresponding shot noise in the SIM reconstructed image by multi-photon TF excitation. Thus, ITF makes optical sectioned super-resolution images practically available in deep imaging or dense scattering media. Three-dimensional ITF (3D-ITF) microscopy [17] as shown in Fig. 1 adds axial spatial modulation in illumination [14] to further improve the sectioning ability and the axial resolution compared to Two-dimensional ITF (2D-ITF), which has only lateral spatial modulation, at the cost of more raw-image acquisition but with the same setup complexity. There are methods like ITF, such as combining HiLo [18] with TF. These methods require fewer raw images to remove scattered and out-of-focus emission but lose the spatial resolution improvement [19-21].

ITF is classified as a nonlinear SIM [11,12] because harmonics in the modulation frequency of the interferometric pattern are generated through multi-photon excitation as shown in Figs. 2 (a) and (g). However, ITF does not offer better resolution than regular SIM. There are two reasons for that low resolution. First, as one type of two-photon excitation fluorescence (TPEF) microscopy, the excitation wavelength in 3D-ITF is around two times as long as the emission wavelength; thus, the possible maximum spatial modulation frequency is around the cut-off spatial frequency of the emission optical transfer function (OTF), which is the same in regular SIM. Secondly, as shown in Fig. 2 (a), the higher the spatial modulation frequency (p, lateral and q, axial) is, the lower the axial spatial frequency support in TF, k_{TF}, is. Thus, there is a trade-off between enhanced spatial resolution and TF sectioning ability. This makes the maximum spatial modulation frequency even lower than the cut-off spatial frequency of emission OTF. In other words,
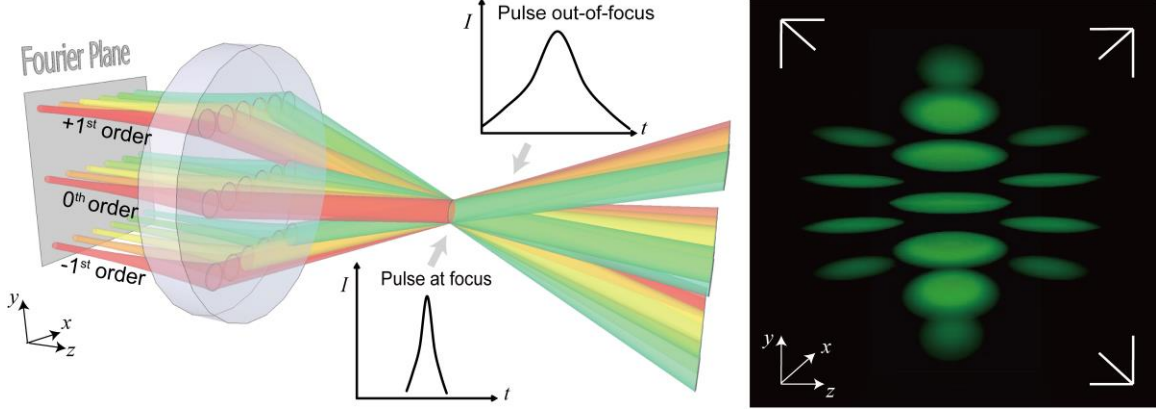
Fig. 1. Schematic of 3D-ITF (left) and its two-photon excitation pattern around focus (right). In 2D-ITF, 0th order spatial chirped light doesn't exist.

the spatial frequency bandwidth of each sub-image of different modulation frequencies is not fully utilized to enhance spatial resolution since there are many useless overlapping areas in the spatial spectrum as shown in Figs. 2 (f) and (g). This is the drawback of ITF in perfect optics. However, the overlap in spatial spectrum of sub-images in fact offers ITF redundancy in the spatial frequency domain. Also, 3D-ITF has more redundancy compared to 2D-ITF as there is more overlapping of spatial frequencies among sub-images. The redundancy can make up for the loss of spatial frequency in TF OTF due to optical distortions so that 3D-ITF has resistance to optical distortions.

To prove the resistance to optical distortions in 3D-ITF, we have to consider not only the distorted emission but also the distorted illumination in 3D-ITF since we don't know whether the present algorithm generates additional image artifacts with distorted illumination in 3D-ITF. How distorted optics influence SIM [22-24] and TF illumination [25-30] has been separately studied, but not yet for ITF microscopy. We extend this study on 3D-ITF microscopy. 3D-ITF illumination mixes chromatic and monochromatic distortions. Longer wavelength is used in deep imaging or dense scattering media. These differ from the distortions in SIM illumination. How optical distortions affect 3D-ITF illumination and how these effects transfer through image reconstruction are analyzed in section 2. Then, considering emission distortion, we derive the distorted PSF of 3D-ITF microscopy for the first time. By this, we verify the redundancy in distorted 3D-ITF and confirm that there are no additional image artifacts due to distorted illumination. The optical distortion in general reduces the image signal-to-noise ratio (SNR) and effectively reduces the cut-off frequency in TF OTF. In section 3, we use simulation to first investigate the resistance of resolution to the reduction of effective cut-off frequency in 3D-ITF. Then we consider the influence of emission wavefront distortion, which is the main optical distortion in 3D-ITF and TF, and study the resolution and noise artifacts at different levels of background fluorescence via simulation. The objective of this paper is to theoretically point out the redundancy in distorted 3D-ITF

images and numerically prove the resistance of resolution and noise artifacts to optical distortions.
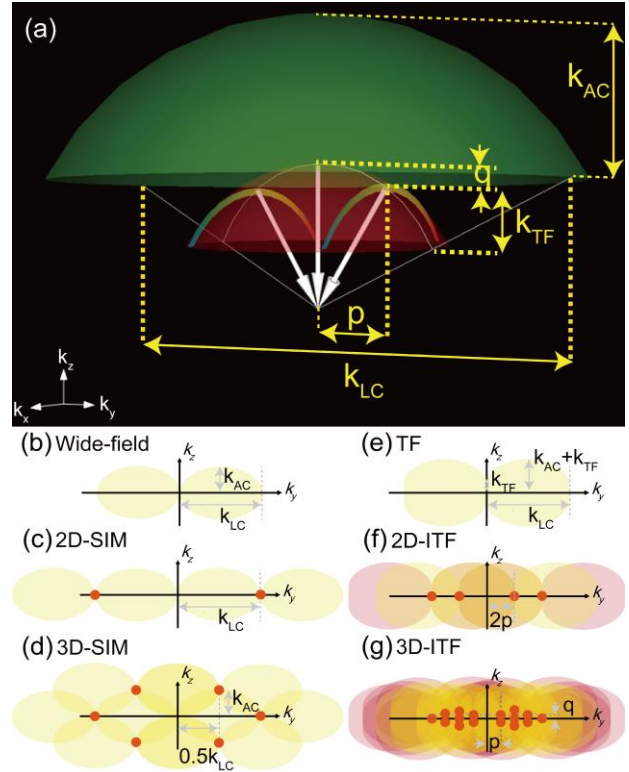

Fig. 2. Redundancy in 3D-ITF OTF. (a) Wave vectors (white vectors) of three diffraction orders in 3D-ITF illumination. The points on red sphere correspond to possible illumination wave vectors in 3D-ITF illumination while the points on green sphere correspond to possible TPEF emission wave vectors in 3D-ITF. Two rainbows correspond to +1st and -1st order TF illumination wave vectors, and there is a trade-off between the axial frequency support in TF, k_{TF} and the fundamental spatial modulation frequency in 3D-ITF, p and q, lateral and axial respectively. (b) OTF in wide-field microscopy, which is also emission OTF. (c, d) OTF in 2D-

SIM (c) and 3D-SIM (d). The red dots indicate the modulation frequencies and the yellow double ellipses indicate the shifted sub-OTFs, which are the same as (b). DC sub-OTF is excluded to remove background fluorescence. There is little frequency overlap in SIM. (e) OTF in TF microscopy, which is an axial convolution of emission OTF and TF sectioning ability. (f, g) OTF in 2D-ITF (f) and 3D-ITF (g). The red double ellipses indicate the shifted sub-OTFs due to two-photon excitation. Both the red and yellow double ellipses are the same as (e). In contrast to SIM, a large number of frequencies overlap in 3D-ITF, and multiple sub-bands overlap. This supports the redundancy in 3D-ITF.

2. Redundancy in distorted 3D-ITF OTF

In this section, we derive the distorted PSF and OTF of 3D-ITF microscopy based upon the principle of SIM and wide-field TF's performance in distorted optics as well as considering the distorted emission light. We first introduce the PSF of 3D-ITF microscopy in perfect optics.

2.1. Method of 3D-ITF and its PSF in perfect optics

As shown in Fig. 1, 3D-ITF microscopy has its own unique illumination [17] composed of three diffracted lines at the back aperture of the objective lens. Each line is composed of dots of different colors that resemble a rainbow. In the spatial domain, the coherent combination at the focal region forms a 3D interferometric pattern the same as 3D-SIM [14]. In the time domain, the patterns of different colors only arrive at the same time at the focal plane. Out-of-focus, different colors have different delays so that the illumination pulse is broadened out-of-focus. This is called TF [1,2]. When the illumination light two-photon excites the sample, TF supports the sectioning ability comparable to a line scanning two-photon excitation microscopy. For a target sample, $S(\mathbf{r})$, the acquired two-photon excited fluorescence raw image divided by the intensity constant is [17]

$$
\begin{aligned}
D_m(\mathbf{r}) &= \sum_{j=-4}^{+4} \int S(\mathbf{r}') \exp\left[i(j\mathbf{p}\mathbf{r}' + j\varphi_m)\right] A_{TF}(z-z') A_j^{(2)}(z-z') h(\mathbf{r}-\mathbf{r}') d\mathbf{r}' \\
&= \sum_{j=-4}^{+4} S(\mathbf{r}) \exp\left[i(j\mathbf{p}\mathbf{r} + j\varphi_m)\right] \otimes \left[A_{TF}(z) A_j^{(2)}(z) h(\mathbf{r})\right]
\end{aligned}
\tag{1}
$$

Here, $\mathbf{p}$ is the fundamental modulation spatial frequency of the interferometric pattern in the lateral direction, φ_m is the corresponding offset phase, j refers to the jth order lateral harmonics inside the interferometric pattern, and i equals $\sqrt{-1}$. Note that the 3D interferometric pattern has two harmonics plus one DC component, while the two-photon excitation process boosts this to four harmonics plus one DC component. $A_{TF}(z)$ refers to the sectioning ability of TF. $A_j^{(2)}(z)$ refers to the axial modulation corresponding to the jth lateral harmonics inside the interferometric pattern. More precisely, it is a combination of harmonics in the axial direction, and details were described in a previous 3D-ITF work [17]. $h(\mathbf{r})$ indicates the PSF of emission light, which passes through the same objective lens used for illumination and then forms the image on the camera in an epifluorescence setting. It describes the performance of the imaging optics for emission light. In image reconstruction, we use the homodyne-detection method. We take multiple raw images, which are counted by indicator m. The difference between m^{th} raw images is their offset phases, which change every $2\pi/9$. In the Fourier domain, the raw image is

$$
\tilde{D}_m(\mathbf{k}) = \sum_{j=-4}^{+4} \tilde{S}(\mathbf{k} - j\mathbf{p}) \exp(ij\varphi_m) \times \left[\tilde{A}_{TF}(k_z) \otimes \tilde{A}_j^{(2)}(k_z) \otimes \tilde{h}(\mathbf{k})\right]
$$

$$
. \tag{2}
$$

To reconstruct the image, we first separate each down-converted sub-band $\tilde{S}(\mathbf{k} - j\mathbf{p})$ from raw images by homodyne detection. Then, we up-convert the sub-band $\tilde{S}(\mathbf{k} - j\mathbf{p})$ to its correct frequency region and compensate for its offset phase φ_m. Thus, the reconstructed image is

$$
\tilde{D}_{3D\text{-}ITF}(\mathbf{k}) = \tilde{S}(\mathbf{k}) \times \left[\sum_{j=-4}^{+4} a_j \tilde{A}_{TF}(k_z) \otimes \tilde{A}_j^{(2)}(k_z) \otimes \tilde{h}(\mathbf{k}+j\mathbf{p})\right] ,
$$

$$
\tag{3}
$$

where a_j is the weighting factor, which can be adjusted to enhance high-frequency support or improve SNR. Here, a_0 is set as 0 to exclude the DC sub-band for background fluorescence subtraction [17]. Note that instead of simple weighting in Eq. (3), we can use the Weiner filter to achieve flat synthesized bandwidth. From Eq. (3), we know that the effective OTF of 3D-ITF microscopy is

$$
\tilde{h}_{3D\text{-}ITF}(\mathbf{k}) = \sum_{j=-4}^{+4} a_j \tilde{A}_{TF}(k_z) \otimes \tilde{A}_j^{(2)}(k_z) \otimes \tilde{h}(\mathbf{k}+j\mathbf{p}) . \tag{4}
$$

By inverse Fourier transform, it is the effective 3D-ITF PSF,

$$
h_{3D\text{-}ITF}(\mathbf{r}) = \left[\sum_{j=-4}^{+4} a_j \exp(-ij\mathbf{p}\mathbf{r}) A_j^{(2)}(z)\right] \times h_{TF}(\mathbf{r}) , \tag{5}
$$

where

3

$$h_{TF}(\mathbf{r}) = A_{TF}(z)h(\mathbf{r}) . \quad (6)$$

The left part of Eq. (5) contains the super composition of harmonics in lateral and axial directions, which is almost a replica of the two-photon excitation pattern of the 3D interferometric pattern but reorganizes the weighting. This part offers us the super-resolution imaging. The right part of Eq. (5), $h_{TF}(\mathbf{r})$, is the PSF of TF microscopy, and is the product of TF sectioning ability and emission PSF as shown in Eq. (6). In TF PSF, TF sectioning ability only affects the axial direction to narrow the shape of emission PSF. Numerically, the full width at half maximum (FWHM) of the TF sectioning ability is much larger than the axial FWHM of the emission PSF, so the TF PSF is dominated by the emission PSF.

2.2. 3D-ITF PSF and OTF in distorted optics

Now, we consider the effects of optical distortions. In imaging practice, the sample and environment differ from the ideal conditions. Substantial distortions arise from the mismatch of the refractive index among sample, immersion media, mounting media and objective lens, and the inhomogeneous refractive index distribution of the sample itself. These distort the wavefront so that the phase of the spatial frequency is modulated in pupil function [31-34]. Another type of distortion arises from absorption and small-scale particle-induced scattering, such as Rayleigh scattering, and it mainly attenuates the ballistic photons. Since the high spatial frequency components have more loss due to a longer journey inside absorption and scattering media, effectively they reduce the spatial frequency bandwidth [35]. The third type of distortion is large-scale particle-induced scattering, such as Mie scattering or forward scattering, which usually happens in tissue with longer wavelength [36]. In addition to the previous effects, it diffuses the spatial frequency. High spatial frequency has more chance to shift to low spatial frequency than vice versa due to a longer pathway in the scattering media.

For distorted illumination light, analysis becomes complicated as multiple colors are involved. To handle this, we will transfer the chromatic effects as temporal effects. Statistically, we first classify the illumination light as ballistic light and scattered light. Ballistic light is only wavefront-distorted and attenuated. For ballistic light, each dispersed colorful dot at the back aperture of the objective lens is coupled to a spatial frequency as shown in Fig. 1 and 2 (a). The common phase alteration of the dispersed dots inside each diffracted line is effectively viewed as a result of monochromatic wavefront distortion. In fact, in 3D-ITF, we have three diffraction orders as illumination light so that the monochromatic wavefront distortion contains only three phase variations corresponding to +1, 0 and -1 diffraction orders. As with SIM, these change the offset phases of the interferometric pattern, which leads to a spatial shift [23]. Variation in offset phase is not a problem if we regard the

offset phase as an unknown parameter. We can search the offset phase by maximizing the cross correlation of the real part and absolute part of the corresponding sub-band image [15] or by other computational algorithms [37,38].

The remaining phase alterations of the dispersed dots inside each diffracted line are effectively viewed as chromatic wavefront distortion, which is a spectrum phase modulation. This chromatic characteristic does not only originate from the difference of refractive index but mainly from the difference of pathway. Different dots of color have different pathways and thus face different manners of scattering, refraction and absorption. The effective chromatic distortions stretch and distort the temporal profile of the 3D interferometric pattern so as to degrade the TF sectioning ability [25-30]. We use distorted TF sectioning ability, $A_{dTF}(z)$, to describe it.

For 3D-ITF illumination, scattered light, as non-ballistic light, is mainly a result of forward scattering, which dominates the scattering process in tissue imaging and for longer wavelength [36]. Forward scattering, or small-angle scattering, detunes the spatial frequency of illumination light. Statistically, the phases of detuned light of different colors, especially from different diffraction orders, are mostly uncorrelated. Thus, in the time domain, the scattered light barely forms a short pulse compared to ballistic light, and its contributions are further suppressed by two-photon excitation. Thus, the modulation frequency of the interferometric pattern is not altered by forward scattering. This characteristic of locking spatial frequency was reported in a previous TF work [28]. On the contrary, statistically the phases of detuned light of neighboring colors inside the same diffraction order are mostly correlated. The scattered light contributes to the DC component of the interferometric pattern and diffuses the DC component in the spatial spectrum. The light as speckles transfers to the 0th order image, the sub-image with $j = 0$ in Eq. (1). By homodyne detection, we can successfully separate the altered 0th order image from other orders' images. To eliminate the error, we simply don't use the 0th order image in image reconstruction. Indeed, the scattered and out-of-focus emission light is hidden in the 0th order image, and is also removed by excluding the 0th order image. Thus, with distorted illumination, the image reconstruction algorithm is still valid. Through image reconstruction, the super-composition of harmonics will be retained in Eq. (5) with optical distortions.

Then, we consider the distorted emission light, which is the same in other wide-field microscopy. In perfect optics, as an incoherent imaging, the emission OTF, $\tilde{h}(\mathbf{k})$ is the autocorrelation of the pupil function of the objective lens. With distorted optics, we model a distorted emission OTF, $\widetilde{h_d}(\mathbf{k})$. The loss of amplitude due to Rayleigh scattering, imperfect optics and misalignment could be modeled as a non-uniform pupil function or simply as lower effective numerical aperture (NA). The wavefront distortion could be modeled as adding the phase with corresponding Zernike polynomials to the pupil function. Both result in narrower

bandwidth for the emission OTF and thus the distorted emission PSF, $h_d(\mathbf{r})$ is broadened. In addition, the OTF spectrum is wavefront-distorted so that there are distorted emission PSF shapes such as side lobes or double peaks [31,32,34]. These effects will be discussed in detail in section 3.3.

The number of optical distortions is usually depth-dependent and thus the distorted TF sectioning ability,

$$D_m(\mathbf{r}) = \sum_{j=-4}^{+4} \int S(\mathbf{r}') \exp\left[i(j\mathbf{p}\mathbf{r}' + \varphi_{m,j})\right] A_{dTF}(z-z',z) A_j^{(2)}(z-z') h_d(\mathbf{r}-\mathbf{r}',z') d\mathbf{r}' . \quad (7)$$

In the z' domain, the integration is approximately non-zero around only the TF-sectioned image plane at depth z. Thus, the integration is affected by only the in-focus distorted emission PSF around depth z, so the distorted emission PSF in Eq. (7) can be replaced by $h_d(\mathbf{r}-\mathbf{r}',z)$, which replaces its depth argument z' with z. For the targeted details such as cells or synapses located at depth z_0, only the sectioned

$A_{dTF}(z)$, and the distorted emission, PSF, $h_d(\mathbf{r})$, are depth-dependent functions as $A_{dTF}(z,z')$ and $h_d(\mathbf{r},z')$ respectively where z' is the depth argument [23]. Here, we don't consider the lateral dependency of distortion because the path-length difference in the sample is negligible within the ~100-μm field of view. As a summation of previous analysis, with distorted optics, Eq. (1) should be revised as

images at depth $z \approx z_0$ are required to build up their 3D image. Thus, the depth argument z in the distorted TF sectioning ability, $A_{dTF}(z-z',z)$, and the distorted emission PSF, $h_d(\mathbf{r}-\mathbf{r}',z)$, could be replaced by z_0 in order to evaluate the effective PSF of the targeted details. With these replacements, Eq. (7) can still be written as a form of convolution as

$$D_m(\mathbf{r}) = \sum_{j=-4}^{+4} \int S(\mathbf{r}') \exp\left[i(j\mathbf{p}\mathbf{r}' + \varphi_{m,j})\right] A_{dTF}(z-z',z_0) A_j^{(2)}(z-z') h_d(\mathbf{r}-\mathbf{r}',z_0) d\mathbf{r}'$$
$$= \sum_{j=-4}^{+4} S(\mathbf{r}) \exp\left[i(j\mathbf{p}\mathbf{r} + \varphi_{m,j})\right] \otimes \left[A_{dTF}(z,z_0) A_j^{(2)}(z) h_d(\mathbf{r},z_0)\right] \quad . \quad (8)$$

Through the same analysis from Eq. (1) to Eq. (6), we derive the distorted 3D-ITF PSF from Eq. (8) as

$$h_{d3D\text{-}ITF}(\mathbf{r},z_0) = \left[\sum_{j=-4}^{+4} a_j \exp(-ij\mathbf{p}\mathbf{r}) A_j^{(2)}(z)\right] \times h_{dTF}(\mathbf{r},z_0) , \quad (9)$$

where the distorted TF PSF is

$$h_{dTF}(\mathbf{r},z_0) = A_{dTF}(z,z_0) h_d(\mathbf{r},z_0) . \quad (10)$$

Here, the distorted 3D-ITF PSF and the distorted TF PSF are both depth-dependent functions. We will drop the depth argument as it doesn't affect further analysis. This can be picked up at any further equation. Compared to Eq. (5) and Eq. (6), the distorted optics only influence the TF PSF. For spectrum view, the distorted 3D-ITF OTF is a Fourier transform of Eq. (9) as

$$\tilde{h}_{d3D\text{-}ITF}(\mathbf{k}) = \left[\sum_{j=-4}^{+4} a_j \tilde{A}_j^{(2)}(k_z) \otimes \delta(\mathbf{k}+j\mathbf{p})\right] \otimes \tilde{h}_{dTF}(\mathbf{k}) , \quad (11)$$

where the distorted TF OTF is

$$\tilde{h}_{dTF}(\mathbf{k}) = \tilde{A}_{dTF}(k_z) \otimes \tilde{h}_d(\mathbf{k}) . \quad (12)$$

Equation (11) means that the distorted 3D-ITF OTF is a summation of shifted distorted TF OTFs. The left part of Eq. (11) refers to the spatial frequencies where the distorted TF OTFs are shifted. These positions are labeled as red points in

Fig. 2 (g). As Fig. 2 (a) shows, in 3D-ITF, because of the limitation of the circular shape of the objective lens, a higher fundamental modulation frequency, $\mathbf{p}$, leads to lower axial frequency support in TF, $\mathbf{k_{TF}}$. Correspondingly, a better 3D-ITF resolution leads to worse sectioning ability in TF. For a trade-off between them, we set the fundamental modulation frequency, $\mathbf{p}$, as around 1/6 the cut-off frequency of the TF OTF, $\mathbf{k_{LC}}$ in the previous experiment [17]. Note that a decrease of around 50% originates from the difference between the excitation and emission wavelength, while another 50% decrease comes from using a 3D-SIM scheme instead of 2D-SIM. Also, a 2/3 decrease originates from the trade-off in geometrical design. In the axial direction, the fundamental modulation frequency, $\mathbf{q}$, is around 1/10 the cut-off frequency of the TF OTF [17]. The relatively small value of the fundamental modulation frequency compared to SIM and the multiple harmonics offers many overlapping areas in the OTF spectrum among sub-TF OTFs. With this unique characteristic, once the distorted TF OTF loses part of its spectrum, the surrounding shifted TF OTFs can utilize the copies of the lost spectrum, which are taken from different spectrum regions of distorted TF OTF to recover the spectrum loss. There is less possibility of losing all the spectrum in distorted TF OTF, such that there is always at least one sub-TF OTF to be able to recover the spectrum loss. This is the redundancy in 3D-ITF. Next, we will investigate how the optical distortions affect image resolution and remaining noise artifacts in TF and 3D-ITF by simulation.

3. Resistance to optical distortions in 3D-ITF

3.1. Simulation condition

In this simulation, a point object is used to evaluate both the spatial resolution and noise artifacts. The excitation wavelength is 1,060 nm and the emission wavelength is 560 nm. The objective lens has a numerical aperture of 1.2 with water immersion (n=1.33). The cut-off frequency of the emission OTF is 26.9 rad/µm and 8.5 rad/µm in the lateral and axial directions respectively. The FWHM of the sectioning ability in TF is 2.7 µm, which corresponds to a bandwidth of 2.3 rad/µm. The fundamental modulation frequency is 4.1 rad/µm and 1.2 rad/µm in the lateral and axial directions respectively. The weighting of the modulation frequencies is set by maximizing the total AC weighting inside the two-photon excitation interferometric pattern. In 3D-ITF, the interferometric pattern with three directions at 0°, 120° and 240° is used. In each direction, nine raw images are simulated. The spatial averaged and temporal integrated two-photon excitation energy in each 3D-ITF raw image is 1/27 times that in TF microscopy. It guarantees the summation of the 27 raw images' two-photon excitation energy is the same as that of the TF image. Thus, the SNR (shot noise) of the summation image of 3D-ITF raw images is the same as the SNR in the TF image. In post processing, a 3D Wiener filter and apodization filter, which was introduced in 3D-SIM [14], are used in both 3D-ITF and TF images. The 3D Wiener filter is constructed by the distorted 3D emission OTF. It corrects the distorted emission OTF in both cases and smooths the synthesized spectrum in 3D-ITF OTF. The apodization filter is constructed by a 3D triangular function with cut-off frequency of the maximum spatial frequency support in TF microscopy and 0.77 times the maximum spatial frequency support in 3D-ITF microscopy to ensure an isotropic spectrum distribution.

3.2 Resistance of spatial resolution to reduction of cut-off frequency

In deep and dense sample imaging, optical distortions increase background fluorescence, which decreases the image SNR. On the other hand, the intensity of the high spatial frequency in TF OTF is relatively low. Thus, the measurable cut-off frequency is reduced by the noise even if the TF OTF is not distorted by the optical distortion. Once the TF OTF bandwidth is reduced by the optical distortion, we expect even lower effective cut-off frequency for an acceptable SNR. Here, we investigate how the spatial resolution reacts to the reduction of the effective cut-off frequency. Figure 3 shows that the lateral and axial resolutions in 3D-ITF degrade much more slowly than those in TF. This simulation roughly shows the resistance of spatial resolution to optical distortions in 3D-ITF.
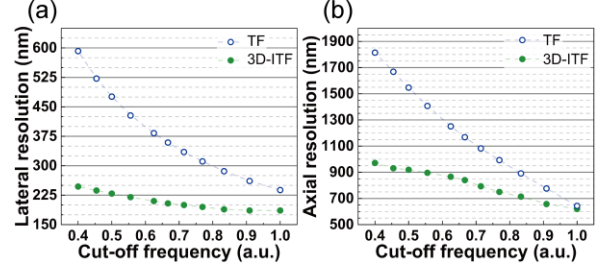

Fig. 3. Spatial resolution degradation with cut-off frequency reduction. (a) Lateral resolution of TF and 3D-ITF; (b) axial resolution of TF and 3D-ITF.

3.3 Wavefront distortion effect and lossless OTF spectrum in 3D-ITF

Next, we consider the effect of the wavefront distortion, which is regarded as the main optical distortion. For wide-field TF, it has been reported that the wavefront distortion has little effect on TF sectioning ability, $A_{TF}(z)$. The degradation occurs for only specified Zernike mode aberration, and the degradation is less than 1.2 times for 1-rad (RMS) Zernike mode amplitude [30]. On the other hand, the wavefront distortion in emission light dramatically degrades and distorts the emission PSF. For 2-rad (RMS) emission Zernike mode amplitude, which equals around 1 rad in illumination, the resolution could degrade several times. Thus, in TF OTF, the main effect comes from the distorted emission OTF. Therefore, we focus on the emission wavefront distortion in the simulation.

Emission wavefront distortion has two effects on TF OTF. Figure 4 shows an example with astigmatism (Zernike mode 5). The first effect is to narrow the OTF bandwidth. With reduced bandwidth, the spatial resolution degrades in TF as Figs. 4 (c) and (d) show. The second effect is to distort the OTF spectrum. As Fig. 4 (a) shows, the astigmatism has an OTF in a cross shape, which is anisotropic. This distortion in the OTF spectrum leads to an axial double peak in PSF as Fig. 4 (d) shows. In contrast, in 3D-ITF, thanks to the redundancy, the lost spectrum caused by the wavefront distortions is recovered by the redundancy. Thus, the whole spectrum is relative uniform and isotropic as Figs. 4 (e) and (f) show. Therefore, we know that the 3D-ITF's OTF spectrum is relatively lossless with distorted optics compared to that in TF.
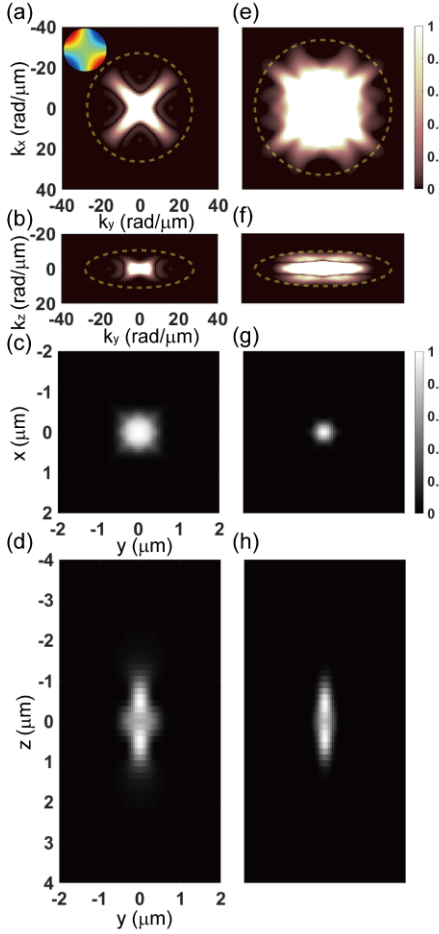
Fig. 4. OTF and PSF with wavefront distortion before using Weiner filter and apodization filter and without considering background fluorescence and shot noise. (a) OTF$_{xy}$ and (b) OTF$_{zy}$ in TF with Zernike mode magnitude of 2 rad (RMS), (c) corresponding PSF$_{xy}$ and (d) PSF$_{zy}$. (e) OTF$_{xy}$ and (f) OTF$_{zy}$ in 3D-ITF with Zernike mode magnitude of 2 rad (RMS), (g) corresponding PSF$_{xy}$ and (h) PSF$_{zy}$. In (a, b, e, f) OTF is normalized by the maximum magnitude and the plot is saturated at 0.05; the dashed yellow circle shows the cut-off frequency of the apodization filter. The wavefront distortion is astigmatism (Zernike mode 5). The insert in (a) shows the phase modulation of Zernike mode 5.

3.4 Trade-off between resolution and remaining noise artifact considering background fluorescence and shot noise

Next, for the practical imaging, we should consider the shot noise. Secondly, we must consider the background fluorescence in deep and dense sample imaging, as well as their shot noise. The bias of the noise (mean value) can be removed, but the variance of the noise such as shot noise will remain, such that the noise artifacts will occur in the processed image. The peak photon number in the TF image without distortion is 27,000 in simulation. In each 3D-ITF

raw image without distortion, the average peak photon number is 1,000. With emission wavefront distortion, the two-photon excitation energy doesn't change, but the peak photon number in the raw image decreases. The background fluorescence contains the out-of-focus and scattered emission. In simulation, a background fluorescence of one magnitude means that the background fluorescence is simulated by additive white Gaussian noise with a mean of 27,000 photons and variance of 2,700 photons in the TF image. The same amount of noise is equally distributed in 27 raw images in 3D ITF microscopy. For any other background magnitude, it scales the background photon number with corresponding magnitude. By adjusting the magnitude of background, we simulate the condition at different imaging depths.

In each simulation condition, we set a threshold SNR value, and we search for the spatial resolution that satisfies the request by adjusting the noise suppression parameter in the Wiener filter. Signal value is the peak intensity of the point object after image processing and noise-bias reduction. Noise value is estimated by the square root of the variance in the spatial region far away from the point object. The acceptable SNR is set as 10 dB for the TF image and 20 dB for the 3D-ITF image. Figure 5 shows the results with either astigmatism or spherical aberration at different imaging depths for TF and 3D-ITF. The spatial resolution is almost the same in 3D-ITF but degrades in TF with wavefront distortion. Moreover, with increasing imaging depth, 3D-ITF still maintains the spatial resolution while the TF image further degrades. Note that 3D-ITF retains a spatial resolution beyond diffraction limitation with distorted optics in deep and dense sample imaging. This shows the resistance of 3D-ITF in practical imaging.
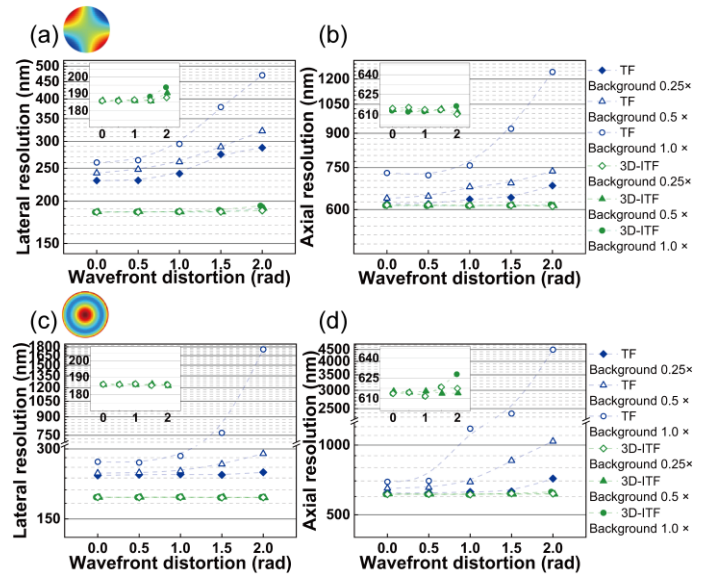

Fig. 5. Spatial resolution degradation with wavefront distortion and background fluorescence. (a) Lateral resolution change and (b) axial resolution change for

7

astigmatism (Zernike mode 5). (c) Lateral resolution change and (d) axial resolution change for spherical aberration (Zernike mode 11). The insert is enlarged view for resolution change in 3D-ITF. The top left corner in (a, c) shows the phase modulation of corresponding Zernike mode.
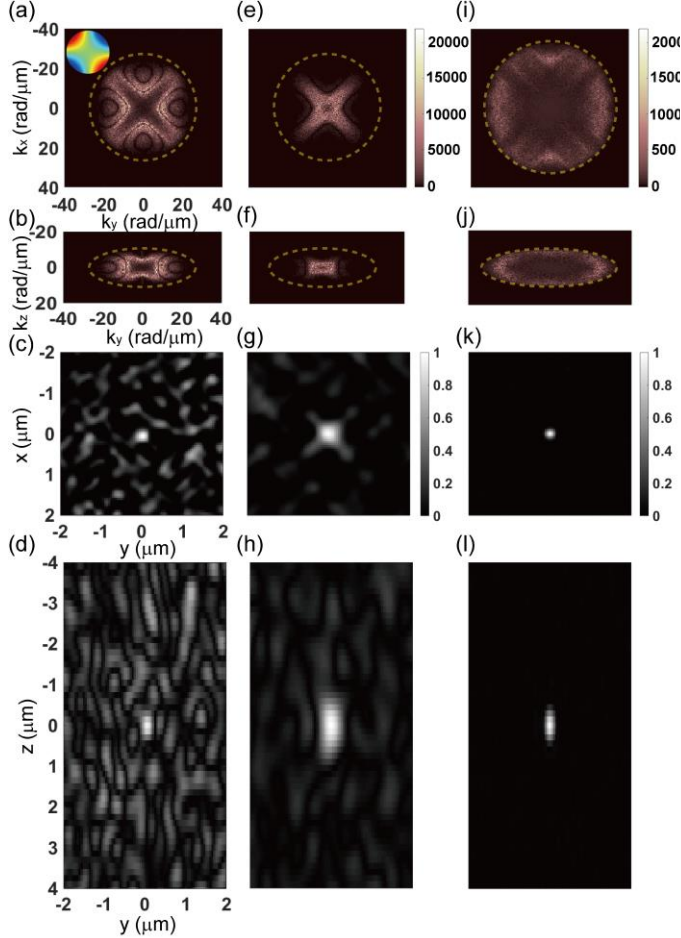

Fig. 6. Trade-off between amplified noise and spatial resolution with Zernike mode amplitude of 2 rad (RMS) and background fluorescence level of 1. (a) OTF_{xy} and (b) OTF_{zy} in TF when SNR=10 dB, (c) corresponding PSF_{xy} and (d) PSF_{zy}; (e) OTF_{xy} and (f) OTF_{zy} in TF when SNR=7 dB, (g) corresponding PSF_{xy} and (h) PSF_{zy}; (i) OTF_{xy} and (j) OTF_{zy} in 3D-ITF when SNR=20 dB, (k) corresponding PSF_{xy} and (l) PSF_{zy}. In (a, b, e, f, i, j) the dashed yellow circle shows the cut-off frequency of the apodization filter. The wavefront distortion is astigmatism (Zernike mode 5). The insert in (a) shows the phase modulation of Zernike mode 5.

In a Wiener filter, the noise artifacts can be suppressed at the cost of losing weak spatial spectrum. As a general rule, since the weak spatial spectrum region has relatively low SNR, we can improve the whole-image SNR by reducing its weighting in the whole-image spectrum. In the TF image, the weak spectrum region plays the short board role in the Barrel

principle. Compare Figs. 6 (a) and (b) to Figs. 4 (a) and (b); this shows that when we increase the weighting of weak spectrum components (the black part in Figs. 4 (a) and (b)) to recover the degraded resolution as well as the distorted PSF shape, the strong spectrum component of the point object (the white part in Figs. 4 (a) and (b)) becomes relatively weak (the inner black part in Figs. 6 (a) and (b)) in the corrected image spectrum, including the corrected object spectrum and noise spectrum. This means the noise mixed in the weak spectrum component of the point object is relatively amplified. To satisfy the SNR request, we have to reduce the weighting of weak spectrum to suppress the amplified noise as Figs. 6 (e) and (f) show. However, this degrades the spatial resolution. On the other hand, the redundancy fixes the short board for 3D-ITF, thus supporting better trade-off between spatial resolution and noise artifacts after the Weiner filter. As Figs. 6 (i) and (j) show, the amplified noise in 3D-ITF is much less than that in TF and is mainly located around the cut-off frequency. Part of the amplified noise is automatically removed by the apodization filter.

In addition to the resistance of spatial resolution, Fig. 7 shows that 3D-ITF also has the resistance of sectioning ability. The sectioning ability is determined by the axial frequency support along the k_z axis, which is called the missing cone in wide-field microscopy as Fig. 2 (b) shows. In 3D-ITF, it is the shifted TF OTF's axial frequency support along the k_z axis that offers the improved sectioning ability. When there is loss in the TF OTF spectrum, it can reduce the sectioning ability, which is the case in 3D-SIM. Again, the redundancy in 3D-ITF recovers the loss of frequency in TF OTF and maintains the frequency support along the k_z axis in 3D-ITF as Fig. 4 (f) shows, such that the sectioning ability in 3D-ITF is resistant to wavefront distortion and background fluorescence. Importantly, this sectioning ability in distorted 3D-ITF is maintained far beyond that with the TF focusing effect only. On the contrary, the TF image loses the sectioning ability due to a large amount of noise artifacts in deep and dense sample imaging.
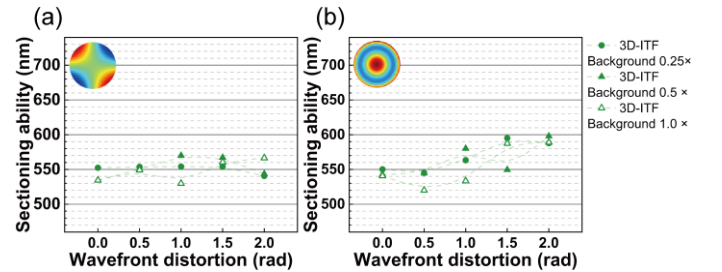

Fig. 7. Sectioning ability with wavefront distortion and background fluorescence in 3D-ITF (a) with astigmatism (Zernike mode 5) and (b) spherical aberration (Zernike mode 11). The insert shows the phase modulation of corresponding Zernike mode.

4. Discussion and Conclusion

In conclusion, the optical distortions in illumination and emission were analyzed for 3D-ITF microscopy to derive its distorted PSF and OTF. With distorted optics, TF illumination locks the spatial modulation frequencies and other illumination distortions, mainly causing the offset shift of the interferometric pattern, retains the image reconstruction algorithm valid. The potential illumination artifacts are removed by eliminating the 0th order image in 3D-ITF. In the distorted 3D-ITF OTF spectrum, the dense sub-TF OTF copies support the redundancy. We show that although the TF OTF spectrum is narrowed and distorted due to optical distortions, the synthesized 3D-ITF OTF spectrum is less affected as the redundancy recovers the loss of spectrum. Thus, 3D-ITF microscopy shows resistance in spatial resolution and sectioning ability with fewer remaining noise artifacts in deep and dense sample imaging, while TF microscopy loses resolution and sectioning ability and retains more noise artifacts.

In practice, in order to increase the usage efficiency of laser power, adaptive optics (AO) [29,39-41] can be combined with 3D-ITF. Indeed, AO can correct wavefront distortion in both illumination and emission independently so as to correct the TF PSF; meanwhile it increases the signal-to-background (SBR) ratio in the raw image. A combination of AO and 3D-ITF microscopy can significantly reduce the time to use AO. As the 3D-ITF image is robust, frequent AO correction during axial scanning is not necessary. This is the scheme to achieve deep and fast volumetric images with robust resolution around or beyond diffraction limitation. In addition, 3D-ITF microscopy can remove the remaining background in microscopy with AO, such as the surface emission in deep imaging, and further suppress the distorted PSF shape due to the remaining high order wavefront distortion. For the same reason, 3D-ITF microscopy can also benefit tissue-clearing techniques [42-44], which directly corrects the mismatch of the refractive index inside the sample.

The resistance of 3D-ITF microscopy prompts us to consider that SIM could be redesigned to increase the robustness of the image in addition to improving the spatial resolution. For example, introducing more modulation frequencies with lower fundamental modulation frequency by using more diffraction orders is a way to increase the redundancy so as to enhance the resistance to distorted optics. Recently, three-photon excitation fluorescence 3D-ITF microscopy was invented to suppress background fluorescence [45]. This scheme is another way to increase the redundancy by increasing the order of modulation harmonics. Importantly, although the increased redundancy requires more raw images to reconstruct the image, the total acquisition time and multi-photon excitation energy are the same in TF microscopy and 3D-ITF microscopy. The usage of TF can also be regarded as a method to increase the robustness of the illumination light, which locks the spatial modulation frequencies and increases the SBR of the raw images. These characteristics are all beyond the original motivation of SIM and TF; future work could include more advanced microscopy such as how to code in order to increase the efficiency of creating redundancy, and how to design in order to increase the ratio of the image SNR to the excitation energy.

.

References

[1] D. Oron, E. Tal, Y. Silberberg, Scanningless depth-resolved microscopy, Opt. Express 13 (2005) 1468-1476.
[2] G. H. Zhu, J. van Howe, M. Durst, W. Zipfel, C. Xu, Simultaneous spatial and temporal focusing of femtosecond pulses, Opt. Express 13 (2005) 2153-2159.
[3] T. Schrödel, R. Prevedel, K. Aumayr, M. Zimmer, A. Vaziri, Brain-wide 3D imaging of neuronal activity in Caenorhabditis elegans with sculpted light, Nat. Methods 10 (2013) 1013-1020.
[4] H. Dana, A. Marom, S. Paluch, R. Dvorkin, I. Brosh, S. Shoham, Hybrid multiphoton volumetric functional imaging of large-scale bioengineered neuronal networks, Nat. Commun. 5 (2014) 3997.
[5] A. Vaziri, C. V. Shank, Ultrafast widefield optical sectioning microscopy by multifocal temporal focusing, Opt. Express 18 (2010) 19645–19655.
[6] Q. Song, A. Nakamura, K. Hirosawa, K. Isobe, K. Midorikawa, F. Kannari, Two-dimensional spatiotemporal focusing of femtosecond pulses and its applications in microscopy, Rev. Sci. Instrum. 86 (2015) 083701.
[7] K. Toda, K. Isobe, K. Namiki, H. Kawano, A. Miyawaki, K. Midorikawa, Temporal focusing microscopy using three-photon excitation fluorescence with a 92-fs Yb-fiber chirped pulse amplifier, Biomed. Opt. Express 8 (2017) 2796-2805.
[8] R. Heintzmann, C. Cremer, Laterally modulated excitation microscopy: improvement of resolution by using a diffraction grating, Optical Biopsies and Microscopic Techniques III, Proc. SPIE 3568 (1999) 185–196.
[9] M. G. L. Gustafsson, Surpassing the lateral resolution limit by a factor of two using structured illumination microscopy, J. Microsc. 198 (2000) 82-87.
[10] J. T. Frohn, H. F. Knapp, A. Stemmer, True optical resolution beyond the Rayleigh limit achieved by standing wave illumination, Proc. Natl. Acad. Sci. U.S.A. 97 (2000) 7232-7236.
[11] R. Heintzmann, T. M. Jovin, C. Cremer, Saturated patterned excitation microscopy—a concept for optical resolution improvement, J. Opt. Soc. Am. A 19 (2002) 1599-1609.
[12] M. G. L. Gustafsson, Nonlinear structured-illumination microscopy: Wide-field fluorescence imaging with theoretically unlimited resolution, Proc. Natl. Acad. Sci. U.S.A. 102 (2005) 13081-13086.
[13] M. A. A. Neil, R. Juskaitis, T. Wilson, Method of obtaining optical sectioning by using structured light in a conventional microscope, Opt. Lett. 22 (1997) 1905-1907.
[14] M. G. L. Gustafsson, L. Shao, P. M. Carlton, C. J. R. Wang, I. N.Golubovskaya, W. Z. Cande, D. A. Agard, J. W. Sedat, Three-dimensional resolution doubling in wide-field fluorescence microscopy by structured illumination, Biophys. J. 94 (2008) 4957-4970.
[15] K. Isobe, T. Takeda, K. Mochizuki, Q. Song, A. Suda, F. Kannari, H. Kawano, A. Kumagai, A. Miyawaki, K. Midorikawa, Enhancement of lateral resolution and optical sectioning capability of two-photon fluorescence microscopy by combining temporal-focusing with structured illumination, Biomed. Opt. Express 4 (2013) 2396-2410.
[16] L.-C. Cheng, C.-H. Lien, Y. Da Sie, Y.Y. Hu, C.-Y. Lin, F.-C. Chien, C. Xu, C.Y. Dong, S.-J. Chen, Nonlinear structured-illumination enhanced temporal focusing multiphoton excitation microscopy with a digital micromirror device, Biomed. Opt. Express 5 (2014) 2526-2536.
[17] K. Isobe, K. Toda, Q. Song, F. Kannari, H. Kawano, A. Miyawaki, K. Midorikawa, Temporal focusing microscopy combined with three-dimensional structured illumination, Jpn. J. Appl. Phys. 56 (2017) 052501.

[18] T. N. Ford, D. Lim, J. Mertz, Fast optically sectioned fluorescence HiLo endomicroscopy, J. Biomed. Opt. 17 (2012) 021105.

[19] H. Choi, E. Y. S. Yew, B. Hallacoglu, S. Fantini, C. J. R. Sheppard, P. T. C. So, Improvement of axial resolution and contrast in temporally focused widefield two-photon microscopy with structured light illumination, Biomed. Opt. Express 4 (2013) 995-1005.

[20] C.-Y Chang, Y. Y. Hu, C.-Y. Lin, C.-H. Lin, H.-Y. Chang, S.-F. Tsai, T.-W. Lin, S.-J. Chen, Fast volumetric imaging with patterned illumination via digital micro-mirror device-based temporal focusing multiphoton microscopy, Biomed. Opt. Express 7 (2016) 1727–1736.

[21] Y. Meng, W. Lin, C. Li, S. Chen, Fast two-snapshot structured illumination for temporal focusing microscopy with enhanced axial resolution, Opt. Express 25 (2017) 23109–23121.

[22] D. D´ebarre, E. J. Botcherby, M. J. Booth, T. Wilson, Adaptive optics for structured illumination microscopy, Opt. Express 16 (2008) 9290-9305.

[23] M. Arigovindan, J. W. Sedat, D. A. Agard, Effect of depth dependent spherical aberrations in 3D structured illumination microscopy, Opt. Express 20 (2012) 6257-6541.

[24] B. Thomas, A. Wolstenholme, S. N. Chaudhari, E. T. Kipreos, P. Kner, Enhanced resolution through thick tissue with structured illumination and adaptive optics, J. Biomed. Opt. 20 (2015) 026006.

[25] H. Dana, S. Shoham, Numerical evaluation of temporal focusing characteristics in transparent and scattering media, Opt. Express 19 (2011) 4937–4948.

[26] E. Papagiakoumou, A. Begue, B. Leshem, O. Schwartz, B. M. Stell, J. Bradley, D. Oron, V. Emiliani, Functional patterned multiphoton excitation deep inside scattering tissue, Nat. Photonics **7** (2013) 274-278.

[27] H. Dana, N. Kruger, A. Ellman, S. Shoham, Line temporal focusing characteristics in transparent and scattering media, Opt. Express 21 (2013) 5677–5687.

[28] A. Bègue, E. Papagiakoumou, B. Leshem, R. Conti, L. Enke, D. Oron, V. Emiliani, Two-photon excitation in scattering media byspatiotemporally shaped beams and their application in optogenetic stimulation, Biomed. Opt. Express 4 (2013) 2869-2879.

[29] C.-Y Chang, L.-C. Cheng, H.-W. Su, Y.Y. Hu, K.-C. Cho, W.-C. Yen, C. Xu, C.Y. Dong, S.-J. Chen, Wavefront sensorless adaptive optics temporal focusing-based multiphoton microscopy, Biomed. Opt. Express 5 (2014) 1768-1777.

[30] B. Sun, P. S. Salter, M. J. Booth, Effects of aberrations in spatiotemporal focusing of ultrashort laser pulses, J. Opt. Soc. Am. B 31 (2014) 765-772.

[31] S.F. Gibson, F. Lanni, Experimental test of an analytical model of aberration in an oil-immersion objective lens used in three-dimensional light microscopy, J. Opt. Soc. Am. A 9 (1992) 154–166.

[32] S. Hell, G. Reiner, C. Cremer, E.H.K. Stelzer, Aberrations in confocal fluorescence microscopy induced by mismatches in refractive index, J. Microsc. 169 (1993) 391–405.

[33] M. Schwertner, M. Booth, T. Wilson, Characterizing specimen induced aberrations for high NA adaptive optical microscopy, Opt. Express 12 (2004) 6540–6552.

[34] E Chaigneau, A. J. Wright, S. P. Poland, J. M. Girkin, R. A. Silver, Impact of wavefront distortion and scattering on 2-photon microscopy in mammalian brain tissue, Opt. Express 19 (2011) 22755-22774.

[35] P. Theer, W. Denk, On the fundamental imaging-depth limit in two-photon microscopy, J. Opt. Soc. Am. A 23 (2006) 3139-3149.

[36] F. Duck, Physical Properties of Tissue: A Comprehensive Reference Network, Elsevier Science, 1990.

[37] S. A. Shroff, J. R. Fienup, D. R. Williams, Phase-shift estimation in sinusoidally illuminated images for lateral superresolution, J. Opt. Soc. Am. A 26 (2009) 413–424.

[38] K. Wicker, O. Mandula, G. Best, R. Fiolka, R. Heintzmann, Phase optimisation for structured illumination microscopy, Opt. Express 21 (2013) 2032–2049.

[39] M. J. Booth, M. A. A. Neil, T. Wilson, Aberration correction for confocal imaging in refractive-index mismatched media, J. Microsc. 192 (1998) 90–98.

[40] N. Ji, Adaptive optical fluorescence microscopy, Nat. Methods 14 (2017) 374–380.

[41] Q. Li, M. Reinig, D. Kamiyama, B. Huang, X. Tao, A. Bardales, J. Kubby, Woofer–tweeter adaptive optical structured illumination microscopy, Photonics Res. 5 (2017) 329-334.

[42] K. Chung, J. Wallace, S.-Y. Kim, S. Kalyanasundaram, A.S. Andalman, T.J. Davidson, J.J. Mirzabekov, K.A. Zalocusky, J. Mattis, A.K. Denisin, S. Pak, H. Bernstein, C. Ramakrishnan, L. Grosenick, V. Gradinaru, K. Deisseroth, Structural and molecular interrogation of intact biological systems, Nature. 497 (2013) 332–337.

[43] H. Hama, H. Hioki, K. Namiki, T. Hoshida, H. Kurokawa, F. Ishidate, T. Kaneko, T. Akagi, T. Saito, T. Saido, A. Miyawaki, ScaleS: an optical clearing palette for biological imaging, Nat. Neurosci. 18 (2015) 1518–1529.

[44] M.-T. Ke, Y. Nakai, S. Fujimoto, R. Takayama, S. Yoshida, T.S. Kitajima, M. Sato, T. Imai, Super-Resolution Mapping of Neuronal Circuitry With an Index-Optimized Clearing Agent., Cell Rep. 14 (2016) 2718–2732.

[45] K. Toda, K. Isobe, K. Namiki, H. Kawano, A. Miyawaki, K. Midorikawa, Interferometric temporal focusing microscopy using three-photon excitation fluorescence, Biomed. Opt. Express 9 (2018) 1510-1519.